Ultrafast magnetization dynamics in half-metallic Co_2FeAl Heusler alloy

R. S. Malik, E. K. Delczeg-Czirjak, R. Knut, I. Vaskivskyi, S. Jana, R. Stefanuik, Y. O. Kvashnin, J. Söderström, and O. Karis

Department of Physics and Astronomy, Uppsala University, Box 516*, SE-*75120*, Uppsala, Sweden*

D. Thonig

*School of Science and Technology, Örebro University, SE-*70182 *Örebro, Sweden*

R. Gupta, S. Husain, A. Kumar, and P. Svedlindh

Department of Materials Science and Engineering, Uppsala University, Box 534*, SE-*75121*, Uppsala, Sweden*

O. Eriksson

Department of Physics and Astronomy, Uppsala University, Box 516*, SE-*75120*, Uppsala, Sweden and*

*School of Science and Technology, Örebro University, SE-*70182 *Örebro, Sweden*

I. SUPPLEMENTAL MATERIAL

S1. Computational Details and Results: Electronic structure calculation, Heisenberg exchange, and Gilbert damping

Density functional theory (DFT)[1,2] in combination with the atomistic spin dynamics method (UppASD)[3] was used to calculate the electronic structure and simulate the dynamical properties of Co_2FeAl for different levels of ordering, ranging from the completely disordered $A2$ phase to the semi-ordered $B2$ phase. Co_2FeAl (CFA) is a full-Heusler alloy, characterized by the X_2YZ formula and it is described within the Fm-3m (225) crystallographic space group. Atoms X, Y and Z occupy the 8c, 4a, and 4b Wyckoff positions, respectively. The level of ordering can be described by the formula:

$$\left[\mathrm{Co}_x\mathrm{Fe}_{\frac{1-x}{2}}\mathrm{Al}_{\frac{1-x}{2}}\right]^X_2\left[\mathrm{Fe}_{0.5-\frac{1-x}{2}}\mathrm{Co}_{1-x}\mathrm{Al}_{0.5-\frac{1-x}{2}}\right]^Y\left[\mathrm{Al}_{0.5-\frac{1-x}{2}}\mathrm{Co}_{1-x}\mathrm{Fe}_{0.5-\frac{1-x}{2}}\right]^Z, \tag{S1}$$

where X, Y, and Z corresponds to the atomic sites described above, and x quantifies the level of ordering between the $A2$- and $B2$ phase. In the completely disordered $A2$ phase, Co, Fe and Al randomly occupy all positions. This is described by $x = 0.5$. The $B2$ phase corresponds to an alloy where Co occupies the 8c (X) position, while Fe and Al are equally distributed between the 4a (Y) and 4b (Z) positions, and is described by $x = 1$. The disordered phases intermediate between the $A2$ and $B2$ ordering are described by $0.5 \leq x \leq 1$. Along this path, $x = 0.5$ corresponds to the $A2$ phase, meaning that 0% $B2$ phase is present, while $x = 1$ is associated with the $B2$ phase, i.e. 100% $B2$. For simplicity, the amount (in %) of $B2$ phase along the $A2$ to $B2$ path will be used below, to describe the ordering when the results are presented and discussed. Note also that Y and Z positions are randomly but equally occupied by the different atomic species, and as a consequence they become equivalent for X in the $A2$ and $B2$ phases and along $A2 \rightarrow B2$ path. Therefore only data for the in-equivalent positions are given in computational results. In the $L2_1$ phase Co occupies the 8c, Fe the 4a and Al the 4b position exclusively.

The electronic structure is obtained solving the Kohn-Sham equations as implemented in the spin-polarized relativistic Korringa-Kohn-Rostoker (SPR-KKR) code[4]. The chemical disorder was treated within the coherent potential approximation (CPA)[5,6]. The Vosko-Wilk-Nusair[7] version of the local spin density approximation was employed as exchange-correlation functional. The density of states (DOS) was derived within the full potential scheme in combination with scalar relativistic calculation. To obtain the Heisenberg exchange integrals and the Gilbert damping parameter, the Dirac equation was solved within the atomic

sphere approximation. For the lattice constant the experimental value[8] is taken. The angular momentum cutoff of $l_{max} = 4$ was used in the multiple scattering expansion. A k-point grid consisting of ≈ 1600 points in the irreducible Brillouin zone was employed for the self-consistent calculations, and more than 1500000 for the Gilbert damping calculations.

The Gilbert damping parameter, α, evaluated at 300 K was calculated via the linear response theory[9]. An alloy analogy model within CPA was considered in order to take into account the temperature effects in the scattering process of electrons with respect to atomic displacement[10]. The "scattering-in" term of the Boltzmann equations was taken into account via vertex corrections[11]. The exchange parameters J_{ij} between the atomic magnetic moments were calculated using the magnetic force theorem implemented in the Liechtenstein-Katsnelson-Antropov-Gubanov (LKAG) formalism[12,13].

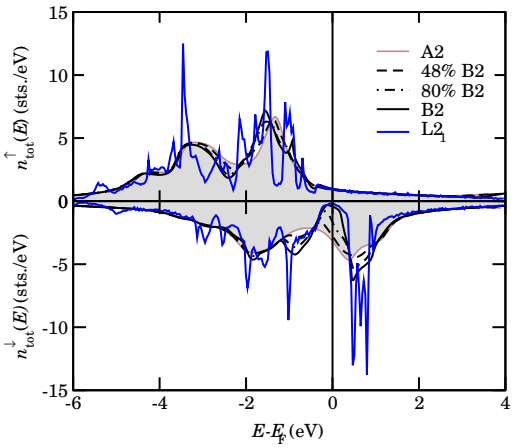

FIG. S1. Majority $n^{\uparrow}(E)$ (upper panel) and minority $n^{\downarrow}(E)$ (lower panel) density of states for completely disordered $A2$ phase (grey shaded area), partially ordered $B2$ phase (black line) and intermediate phases along $A2 \rightarrow B2$ transition (48% $B2$ phase with dashed line and 80% $B2$ phase with dashed-dotted line) of Co_2FeAl. The DOS for $L2_1$ phase is represented with blue line showing a band gap for minority chanel at Fermi level (E_F, shown as a vertical black line).

Evolution of the density of states during the transition from $A2$ to $B2$, is presented in Fig. S1. We can observe a small rearrangement of the electron occupation in the majority channel $n^{\uparrow}(E)$. In contrast, chemical ordering induces a drastic change in the minority channel $n^{\downarrow}(E)$. As Co gradually occupies exclusively the 8c position a gap starts to develop in the minority channel. The gap formation becomes complete in the $L2_1$ phase, as was shown in[14].

Opposite to the recently studied Heulser material Co_2MnGe[15], the density of states does not exhibit strong energy shifts due to crystal ordering, and the

element-resolved density of states (not shown here) reveals similar gaps in the minority channel for Fe and Co. Thus, when a 1.55 eV photon is absorbed by the material, minority carriers in the B2 phase are excited from both Co and Fe states. No imbalance is present in how Co and Fe projected orbitals contribute to the excitation from initial to final states, and, consequently, direct and spin conserving transitions do not produce optically induced angular momentum transfer between atoms. Hence in the following, we will only determine contributions to magnon excitations in the ultrafast magnetism of Co_2FeAl.

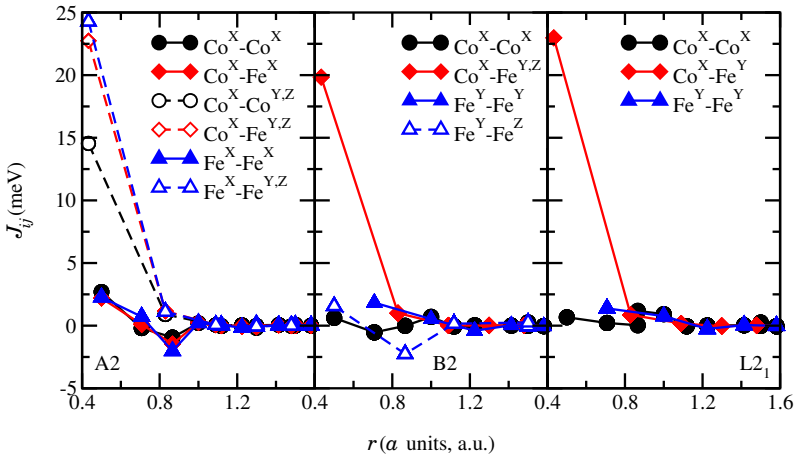

FIG. S2. Magnetic exchange interactions, J_{ij} as a function of distance, r (expressed in lattice parameter units, a). Left, middle and right panel shows J_{ij} for $A2$, $B2$ and $L2_1$ ordering, respectively. Black circles stand for Co-Co interactions between Co atoms sitting on the same/different Wyckoff position (filled/open symbols). Red diamonds label Co-Fe interactions between Co and Fe atoms sitting on the same/different Wyckoff position (filled/open symbols)). Blue triangles belong to Fe-Fe interactions between Fe atoms sitting on the same/different Wyckoff position (filled/opensymbols).

Magnetic exchange interactions are plotted in Fig. S2 for different chemical orderings ($A2$, $B2$ and $L2_1$). The largest J_{ij} value we find for Fe-Fe pairs when they occupy different sublattices in the $A2$ phase (open up-triangles in the left panel of Fig. S2). Strong interactions are also found between Co and Fe atoms, in all phases when they are placed in different Wyckoff positions (see open diamonds in the left panel of Fig. S2 and filled diamonds in the middle and right panel of Fig. S2). Intermediate Co-Co J_{ij} interactions are found only for the $A2$ phase, when the Co atoms are not placed on the same position (open circles, left panel), in all other cases the J_{ij}(Co-Co) has low value. For the strong interactions, J_{ij}(Fe-Fe), J_{ij}(Co-Fe) and J_{ij}(Co-Co) the highest value is for the nearest neighbor interactions, and the strength of J_{ij} decays fast with distance. The weaker, more long ranged,

TABLE S1. Gilbert damping parameters, α, calculated for different chemical ordering of CFA. Element resolved damping parameters are given for Co and Fe for different sublattices.

Phase	Average α	X (8c)		Y,Z (4a, 4b)	
(%)	($\times 10^{-3}$)	Co	Fe	Co	Fe
0($A2$)	2.03	2.78	0.99	2.78	0.99
20	1.99	2.34	1.12	3.32	0.86
40	1.87	1.96	1.22	4.04	0.70
44	1.83	1.88	1.23	4.22	0.67
48	1.79	1.81	1.24	4.41	0.64
52	1.74	1.73	1.25	4.62	0.60
80	1.04	1.09	1.06	5.67	0.27
100($B2$)	0.36	0.63	-	-	0.14
$L2_1$	0.42	0.52	-	-	0.31

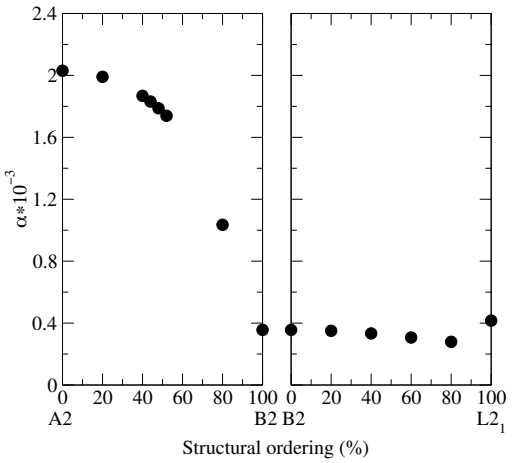

FIG. S3. Calculated Gilbert damping parameters α for differently ordered phases of Co_2FeAl, $A2$, $B2$ and $L2_1$ respectively.

interactions show oscillations which is expected from RKKY interaction. The latter finding is similar to earlier studies, e.g. for Mn-Cu alloys[16].

Calculated Gilbert damping parameters, α, are listed in Table S1 and illustrated in Fig. S3. This parameter has in the past been identified to stand in proportion to the DOS(E_F)[14,17,18]. It may be noted from Table S1 that the damping drops monotonously, but not linearly, along the $A2 \rightarrow B2$ structural path, reaching values for the $B2$ phase that is as low as the value for the $L2_1$ phase. As for the element resolved damping, α(Co) has always larger values than Fe, and its value

is strongly dependent on if Co occupies the X or the Y/Z position. The value of α(Co) is seen to decrease, when Co is on the X position along $A2 \rightarrow B2$ path (the Co concentration increases on the X position in this case). It is also seen to increase when Co occupies the Y/Z position, where its concentration decreases along the $A2 \rightarrow B2$ path. The trend is almost opposite for Fe: α(Fe) drops gradually when Fe is at the Y/Z position, but has a maximum at about 50% $B2$ ordering when Fe is placed in X.

S2. Atomistic spin dynamics; methodology and simulated data

The evolution of atomistic spins is typically determined in terms of precession and dissipation, which is described by the Landau-Lifshitz-Gilbert (LLG) equation [19], here expressed in Landau-Lifshitz (LL) form:

$$\frac{d\vec{m}_i(t)}{dt} = -\frac{\gamma}{(1+\alpha^2)}\left(\vec{m}_i(t) \times \vec{B}_i(t) + \frac{\alpha}{m_i}\vec{m}_i(t) \times (\vec{m}_i(t) \times \vec{B}_i(t))\right). \tag{S2}$$

Here γ is the gyromagnetic ratio, α represents the dimensionless Gilbert damping constant, and $\vec{m}_i = m_i\vec{e}_i$ is an individual atomic moment on site i. The effective magnetic field $\vec{B}_i$ is a superposition of the exchange field $\vec{B}_i^{xc} = -\frac{\partial \mathcal{H}}{\partial \vec{m}_i}$, where $\mathcal{H} = -\frac{1}{2}\sum_{i\neq j} J_{ij}\vec{m}_i \cdot \vec{m}_j$ and the stochastic field $\vec{b}_i$. The latter is describes by a white noise magnetic field term ($\langle \vec{b}_i(t) \cdot \vec{b}_j(t')\rangle = 2D\delta_{ij}\delta(t-t')$), where the fluctuation width is $D = {}^{\alpha k_B T_s}/_{\gamma m}$. Thus, the spin temperature T_s directly passes into LLG equation via the stochastic magnetic field $\vec{b}_i$ and is obtained from solving the two-temperature model (2TM)[20]. The analytical expression of this two temperature model reads,

$$\begin{aligned} T_s = T_0 + & \\ & (T_P - T_0) \times (1 - \exp^{(-t/\tau_{\text{initial}})}) \times \exp^{(-t/\tau_{\text{final}})} + \\ & (T_F - T_0) \times (1 - \exp^{(-t/\tau_{\text{final}})}) \end{aligned} \tag{S3}$$

where T_0 is the initial temperature of the system, T_{P} is the peak temperature after the laser pulse is applied and T_{F} is the final temperature. Both the initial and final temperatures are set to 300 K, where the peak temperature is a parameter in the simulations. The time-dependent parameters τ_{initial} and τ_{final} are exponential parameters, fixed by $\tau_{\text{initial}} = 10$ fs and $\tau_{\text{final}} = 1.5$ ps and they are comparable to those used in[21]. Note that both relaxation times are materials specific and k_{B} is the Boltzmann constant.

Having the Heisenberg exchange and the Gilbert damping parameter calculated from first principles theory, we used them to perform atomistic magnetization

dynamics combined with the two temperature model (2TM) (see Fig.1 of the main text). In the 2TM, the spin temperature increases due to the coupling to the hot-electron bath, that is excited by the external laser pulse. Thermal fluctuations of the spin-system realized in this way cause the magnetization to drop during the first few picoseconds.

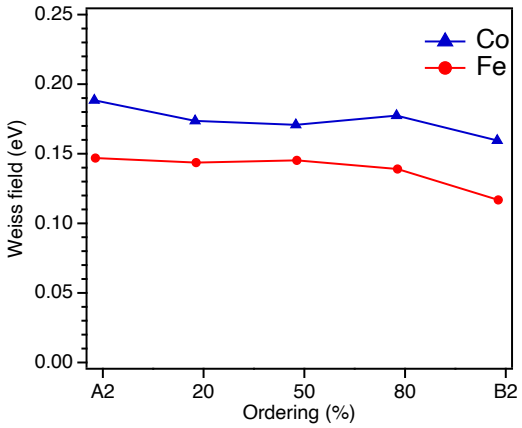

FIG. S4. The calculated Weiss field in phases of CFA with different structural ordering along the $A2 \rightarrow B2$ path.

In order to elucidate what mechanisms that may possibly be responsible for this change, we investigated the local Weiss field, $\vec{B}_i$, along the $A2 \rightarrow B2$ path, since this is the largest term at the right hand side of Eq. (S2). The Weiss field is a direct reflection of the Heisenberg exchange, and it is shown in element projected form in Fig. S4. It may be seen that the Weiss field is quite different for Fe and Co, and interestingly, the Weiss field does not change significantly along the $A2 \rightarrow B2$ path. Hence, small variations in the Weiss field, do not explain the experimental data presented in this investigation.

S3. Thin films growth

The CFA films used in our experiment were grown on Si substrates by means of ion beam sputtering[22]. In these films, different structual ordering, from a disordered ($A2$) phase to a partially ordered ($B2$) phase, can be achieved by varying the growth temperatures T_s[23,24]. We have chosen the sample names by using the different growth temperature . The samples used in this study were CFA_{300K}, CFA_{573K}, CFA_{673K}, and CFA_{773K}, respectively. The structural ordering of these poly-crystalline thin films are estimated as; A2 disorder, 90(5)% B2 order, 90(5)% B2 order and 100(5)% B2 orders for CFA_{300K}, CFA_{573K}, CFA_{673K} and CFA_{773K} thin films , respectively, determined by using the intensity ratio of the (200) and

(220) x-rays diffraction (XRD) peaks[23]. Please note that the precise determination of the ordering parameter employing peak intensity ratio can only be performed in epitaxial films,[17] which is however not the case with our studied films. All of the samples have a 50 nm layer of CFA and 4 nm capping layer of Al to prevent oxidation. The detailed description of the deposition method and the structural properties of the these films are reported in[14,22].

S4. Time-resolved transverse magneto-optical Kerr effect (TR-MOKE)

The magnetization dynamics measurements are carried out by using a transverse magneto-optical Kerr (T-MOKE) pump-probe setup[25]. The laser system is a chirped pulse amplification (CPA)[26], system running at a central wavelength of 800 nm with a maximum energy of 2.5 mJ per pulse and a length of 35 fs.. The time resolved study is achieved by splitting the laser beam into two parts; 80% of the laser beam is used for generating the extreme-ultraviolet (EUV) probe beam and 20% is used as a pump beam. The EUV probe beam is generated by focusing laser light into a gas cell filled with helium. EUV photons in $40 - 72$ eV energies range are generated through a high harmonics generation (HHG) process[27,28]. The IR beam is blocked from reaching the detector with a a 200 nm thick Al filter. The incident angle between the sample and the probe beam is fixed at 45° in order to get maximum magnetic signal in the T-MOKE geometry[29,30]. The delay between pump and probe beam is controlled by a delay stage. An active beam stabilization system is used to avoid any thermal drift in beam path and to ensure the spatial overlap between pump and probe beam. An electromagnet with a magnetic field strength of $\pm$ 80 mT is used to magnetize the sample. Since the infrared (IR) pump and EUV probe are generated from the same laser pulse, the temporal jitter between pump and probe pulses is effectively eliminated. Further details of the experimental setup is reported in[31,32].

A typical pump-probe experiment consists of a series of delay points between pump beam and probe beam. A negative delay corresponds to a situation where the probe arrives on the sample before the pump and magnetization is unchanged. When the pump and probe arrive simultaneously at the sample, is referred to as time zero. For positive delays, the pump arrives first, optically excites the sample and the dynamical response is measured with probe beam. In the -MOKE geometry, the sample is magnetized perpendicularly to the plane of incidence of the incoming p-polarized light, using the above-mentioned in situ electromagnet. The reflected light from the sample is recorded with a charged-coupled device (CCD) camera. In order to detect the T-MOKE signal, spectral changes at the absorption edges of Fe and Co were recorded for two opposite orientations of magnetic field. The measured magnetic asymmetry, A, can be described by

$$A = \frac{I_p^{(+)} - I_p^{(-)}}{I_p^{(+)} + I_p^{(-)}}, \tag{S4}$$

where $I_p^{(+)}$ and $I_p^{(-)}$ are the reflected intensities measured for two different magnetizations. An example of the EUV reflected spectra from a Co_2FeAl thin film is shown in Fig. S5(a). Since Fe and Co have their M-absorption edges at different energies, ∼54 eV and ∼60 eV, respectively, element specific information can be obtained. This is illustrated in Fig. S5(a), where a strong change in intensity of reflected light for two different magnetization directions can be seen at these energies. The measured asymmetry, evaluated from Eq. (S4), is shown as a function of photon energy in Fig. S5(b).

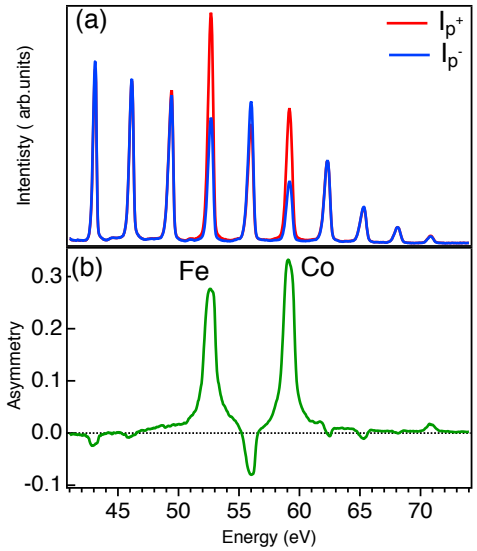

FIG. S5. (a) EUV reflectivity spectra of Co_2FeAl recorded in the T-MOKE configuration at two magnetic field orientations and (b) measured static magnetic asymmetry of Fe (∼54 eV) and Co (∼60 eV).

S5. Ferromagnetic Resonance Measurements (FMR)

Out-of-plane broadband FMR measurements were performed by employing a vector network analyser (VNA), details of this system are presented in[33]. Using field sweep mode, keeping frequency constant in the range of 14 to 24 GHz, the magnetic field dependence of the complex transmission parameter S_{21} was recorded. The recorded field-dependent complex S_{21} data was fitted by using equation[33],

TABLE S2. Measured parameters using ferromagnetic resonance (FMR)

Sample	α(x 10^{-3})	$\mu_0 \triangle H_0$	$g^{\perp}$	$\mu_0 M_{\text{eff}}$(T)
CFA_{300K}	2.91(19)	0.33(11)	2.071(1)	1.1000(06)
CFA_{573K}	2.64(27)	0.30(18)	2.067(2)	1.1324(06)
CFA_{673K}	2.34(38)	0.48(26)	2.065(2)	1.1434(08)
CFA_{773K}	1.13(42)	1.60(29)	2.058(4)	1.1336(14)

$$S_{21}(H,t) = S_{21}^{0} + Dt + \frac{1}{\tilde{\chi}_0}\frac{M_s(H - M_{\text{eff}})}{(H - M_{\text{eff}})^2 - H_{\text{eff}}^2 - \iota\Delta H(H - M_{\text{eff}})} \tag{S5}$$

where S_{21}^{0} corresponds to the non-magnetic contribution to the complex transmission signal, $\tilde{\chi}_0$ is an imaginary function of the microwave frequency. The term Dt accounts for a linear drift of the recorded S_{21} signal and $H_{\text{eff}} = \frac{2\pi f}{\gamma\mu_0}$; f is a microwave frequency, ΔH is full-width half-maximum linewidth, $\gamma = g^{\perp}\mu_B/\hbar$ is the gyromagnetic ratio, $g^{\perp}$ is the Lande spectroscopic splitting factor. Effective magnetization $\mu_0 M_{\text{eff}}$ and γ values were estimated by fitting resonance field $\mu_0 H_r$ vs. frequency f data by using the expression $\mu_0 H_r = \frac{2\pi f}{\gamma} + \mu_0 M_{\text{eff}}$. The S_{21} spectra were fitted to Eq. (S5) shown as red solid lines in Fig. S7, in order to extract the $\mu_0\Delta H$ and $\mu_0 H_r$ values.

The experimentally measured total damping parameter (α_{total}), including both the intrinsic contribution (Gilbert damping) and extrinsic radiative and eddy current damping contributions, was extracted by fitting ΔH vs. f (Fig. S6) to the following expression $\mu_0\Delta H = \frac{4\pi\alpha_{\text{total}} f}{\gamma} + \mu_0\Delta H_0$, where ΔH_0 is the frequency independent linewidth broadening due to sample inhomogeneity. The fitting determined values of all the parameters are presented in Table S2. The α_{total} damping values were corrected for extrinsic contributions using standard methods[33], to determine the intrinsic damping (α) values as presented in the Table S2.

[1] P. Hohenberg and W. Kohn, Phys. Rev. **136**, B864 (1964).

[2] W. Kohn and L. J. Sham, Phys. Rev. **140**, A1133 (1965).

[3] B. Skubic, J. Hellsvik, L. Nordström, and O. Eriksson, J. Phys.: Condens. Mattter. **20**, 315203 (2008).

[4] H. Ebert, D. Ködderitzsch, and J. Minár, Rep. Prog. Phys. **74**, 096501 (2011).

[5] P. Soven, Phys. Rev. **156**, 809 (1967).

[6] G. M. Stocks, W. M. Temmerman, and B. L. Gyorffy, Phys. Rev. Lett. **41**, 339 (1978).

[7] S. H. Vosko, L. Wilk, and M. Nusair, Can. J. Phys. **58**, 1200 (1980).

[8] M. Belmeguenai, H. Tuzcuoglu, M. Gabor, T. Petrisor, C. Tiusan, D. Berling,

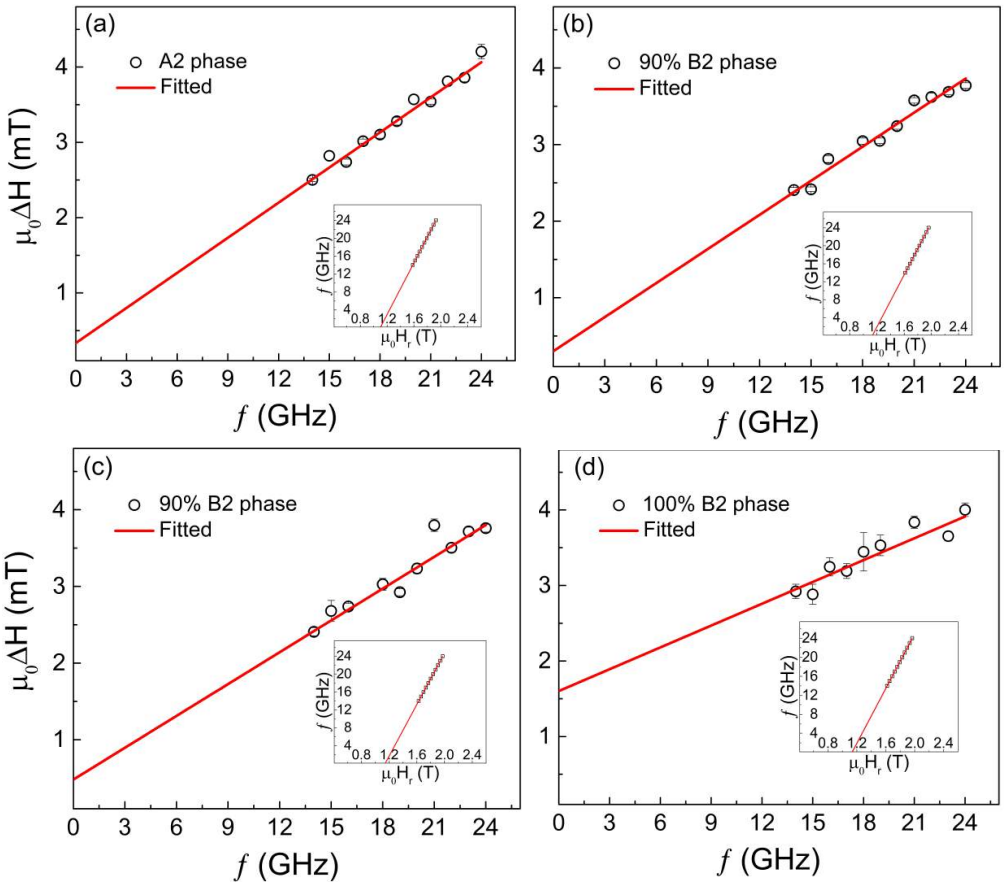

FIG. S6. Linewidth vs. frequency of CFA films deposited at (a) 300 K, (b) 573 K, (c) 673 K , and (d) 773 K. Red lines correspond to fits to the data to extract the experimental Gilbert damping constant. The insets shows the frequency vs. resonance field of these samples.

F. Zighem, and S. M. Chérif, J. Magn. Magn. Mater. **373**, 140 (2015), recent Advances in Nanomagnetism and Spintronics.

[9] H. Ebert, S. Mankovsky, D. Ködderitzsch, and P. J. Kelly, Phys. Rev. Lett. **107**, 066603 (2011).

[10] H. Ebert, S. Mankovsky, K. Chadova, S. Polesya, J. Minár, and D. Ködderitzsch, Phys. Rev. B **91**, 165132 (2015).

[11] W. H. Butler, Phys. Rev. B **31**, 3260 (1985).

[12] A. Liechtenstein, M. Katsnelson, V. Antropov, and V. Gubanov, J. Magn. Magn. Mater. **67**, 65 (1987).

[13] H. Ebert and S. Mankovsky, Phys. Rev. B **79**, 045209 (2009).

[14] A. Kumar, F. Pan, S. Husain, S. Akansel, R. Brucas, L. Bergqvist, S. Chaudhary,

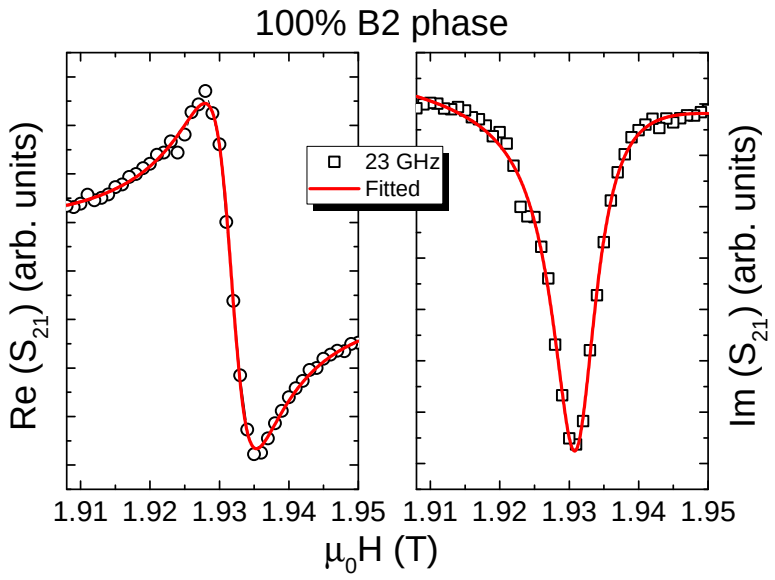

FIG. S7. Re(S_{21}) and Im(S_{21}) vs. μ_0H of CFA_{773K} sample with a 100 % B2 phase at 23 GHz. Black open symbols and red lines correspond to experimental and fitted data, respectively.

and P. Svedlindh, Phys. Rev. B **96**, 224425 (2017).

[15] P. Tengdin, C. Gentry, A. Blonsky, D. Zusin, M. Gerrity, L. Hellbrück, M. Hofherr, J. Shaw, Y. Kvashnin, E. K. Delczeg-Czirjak, M. Arora, H. Nembach, T. J. Silva, S. Mathias, M. Aeschlimann, H. C. Kapteyn, D. Thonig, K. Koumpouras, O. Eriksson, and M. M. Murnane, Sci. Adv. **6** (2020).

[16] I. Turek, J. Kudrnovskỳ, V. Drchal, P. Bruno, and S. Blügel, Phys. Status. Solidi. B **236**, 318 (2003).

[17] S. Mizukami, D. Watanabe, M. Oogane, Y. Ando, Y. Miura, M. Shirai, and T. Miyazaki, J. Appl. Phys. **105**, 07D306 (2009).

[18] J. M. Shaw, E. K. Delczeg-Czirjak, E. R. J. Edwards, Y. Kvashnin, D. Thonig, M. A. W. Schoen, M. Pufall, M. L. Schneider, T. J. Silva, O. Karis, K. P. Rice, O. Eriksson, and H. T. Nembach, Phys. Rev. B **97**, 094420 (2018).

[19] O. Eriksson, A. Bergman, L. Bergqvist, and J. Hellsvik, *Atomistic Spin Dynamics*, Foundations and Applications (Oxford University Press, 2016).

[20] U. Bovensiepen, J. Phys.: Condens. Matter. **19**, 083201 (2007).

[21] R. Chimata, A. Bergman, L. Bergqvist, B. Sanyal, and O. Eriksson, Phys. Rev. Lett. **109**, 157201 (2012).

[22] S. Husain, S. Akansel, A. Kumar, P. Svedlindh, and S. Chaudhary, Sci. Rep. **6**, 28692 (2016).

[23] S. Husain, A. Kumar, S. Akansel, P. Svedlindh, and S. Chaudhary, J. Magn. Magn.

Mater. **442**, 288 (2017).
[24] A. Titov, Y. Jirásková, O. Zivotsky, J. Bursik, and D. Janickovic, AIP. Adv. **8**, 047206 (2018).
[25] S. Jana, J. A. Terschlüsen, R. Stefanuik, S. Plogmaker, S. Troisi, R. S. Malik, M. Svanqvist, R. Knut, J. Söderström, and O. Karis, Rev. Sci. Instrum. **88**, 033113 (2017).
[26] D. Strickland and G. Mourou, Opt. Commun. **55**, 447 (1985).
[27] M. Lewenstein, P. Balcou, M. Y. Ivanov, A. L'huillier, and P. B. Corkum, Phys. Rev. A. **49**, 2117 (1994).
[28] P. B. Corkum, Phys. Rev. Lett. **71**, 1994 (1993).
[29] S. Mathias, C. La-O-Vorakiat, P. Grychtol, P. Granitzka, E. Turgut, J. M. Shaw, R. Adam, H. T. Nembach, M. E. Siemens, S. Eich, C. M. Schneider, T. J. Silva, M. Aeschlimann, M. M. Murnane, and H. C. Kapteyn, Proc. Natl. Acad. Sci. USA. **109**, 4792 (2012).
[30] M. Hecker, P. M. Oppeneer, S. Valencia, H.-C. Mertins, and C. M. Schneider, J. Electron Spectrosc. Relat. Phenom. **144**, 881 (2005).
[31] S. Plogmaker, J. A. Terschlüsen, N. Krebs, M. Svanqvist, J. Forsberg, U. B. Cappel, J.-E. Rubensson, H. Siegbahn, and J. Söderström, Rev. Sci. Instrum. **86**, 123107 (2015).
[32] R. Stefanuik, R. Knut, S. Jana, J. Terschlüsen, A. Sandell, and J. Söderström, Journal of Electron Spectroscopy and Related Phenomena **224**, 33 (2018).
[33] R. Gupta, N. Behera, V. A. Venugopal, S. Basu, A. K. Puri, P. Ström, M. A. Gubbins, L. Bergqvist, R. Brucas, P. Svedlindh, and A. Kumar, Phys. Rev. B **101**, 024401 (2020).